Università degli Studi di Genova

Scuola Politecnica

DIME

Dipartimento di Ingegneria Meccanica, Energetica,

Gestionale e dei Trasporti

Tesi di Laurea in Ingegneria Meccanica

TRANSMISSION OF SOUND THROUGH POROUS MEDIA

Candidato
Rachele Valcalda

Relatore
Prof. Alessandro Bottaro

Correlatore
Dott.ssa Jiasen Wei

Anno accademico 2022/2023

A mamma e papà

Trasmissione del suono attraverso materiali porosi

Sommario

I mezzi porosi sono materiali o sostanze che presentano vuoti o spazi interconnessi all'interno della loro struttura, consentendo in questo modo il passaggio di fluidi. Questi vuoti o pori possono variare in dimensioni, forma e distribuzione nello spazio e si possono trovare sia nei materiali naturali che in quelli artificiali. Esempi di mezzi porosi includono alcuni tipi di rocce, le spugne, le schiume, la carta e persino alcuni tessuti biologici. L'importanza dei mezzi porosi risiede nella loro vasta gamma di applicazioni: in questa tesi ci concentreremo sui rivestimenti acustici utilizzati nel settore aerospaziale per ridurre il rumore del motore. Per studiare come un'onda acustica si propaga attraverso una matrice, abbiamo derivato la sua equazione adimensionale utilizzando il metodo dell'omogeneizzazione, che permette di ottenere un modello macroscopico partendo dallo studio di una cella unitaria. Abbiamo quindi testato il modello risolvendo due tipi di strutture, una isotropa e una non isotropa, in cui i parametri necessari per l'equazione del modello sono stati calcolati risolvendo il problema di chiusura per una cella unitaria. Infine, la precisione del modello è stata verificata con COMSOL Multiphysics®, testando anche come la porosità della struttura e la frequenza dell'onda acustica influenzino il risultato finale.

Transmission of sound through porous media

Abstract

Porous media are materials or substances that have voids, gaps, or interconnected spaces within their structure, allowing the passage of fluids. These voids or pores can vary in size, shape and distribution, and can be found in both natural and artificial materials. Examples of porous media include soil, rocks, sponges, foams, paper, and even some biological tissues. The importance of porous media lies in their wide range of applications across various fields: in this thesis, we will focus on acoustic liners used in aerospace to reduce engine noise. To study how an acoustic wave propagates through an array, we derived its non-dimensional equation using the homogenization method, which allows us to obtain a macroscopic model starting from the study of a unit cell of the matrix. Then we tested the model by solving two structures, an isotropic and a non-isotropic one, where the parameters needed for the model equation are calculated by solving the closure problem for a unit cell. Lastly, the precision of the model is verified with COMSOL Multiphysics®, testing also how the porosity of the structure and the frequency of the acoustic wave influence the final result.

Nomenclature

$\delta\Omega$	boundary of the solid and of the unit cell
γ_s	solid boundary
λ	ratio length-width
Ω	unit cell area
ω	angular frequency
Ω_f	fluid region area
ϕ	porosity
ρ	density
τ_{ij}	viscous stress tensor
$\mathbf{r}$	general coordinates
$\mathbf{x}$	macroscopic coordinates
$\mathbf{y}$	microscopic coordinates
a	rectangle length
b	rectangle width
c	number of rectangles in a row
c_0	speed of sound
d	number of rectangles in a column
e	specific internal energy
f	frequency
k	wave number

k_{eff}	k of an isotropic effective medium
L	matrix length
l	unit cell length
n	number of cylinder in a row
p_i	imaginary part of the pressure
p_r	real part of the pressure
P_{ij}	fluid stress tensor
q	heat flux
R	radius
u	square length
v	velocity
z	rectangle sides unit

Contents

Chapter 1

Introduction

1.1 Background

Porous materials can be commonly found in nature. One example is the sea sponge, which has a substantial volume occupied by void spaces. This unique character allows it to filter water through its pores and capture the particulate matter as food. Similarly, certain types of rocks exhibit porous characteristics. The pumice, for example, emerges as a consequence of entrapped gas bubbles within rapidly cooled magma. Pumice serves practical purposes in construction as concrete blocks and as an abrasive material in both industrial and consumer applications. Wood is also a type of natural porous material as trees have pores throughout the fibrous structural tissue that allow them to take in air and release oxygen. Many other examples can be found in nature, like eggshells and bones.

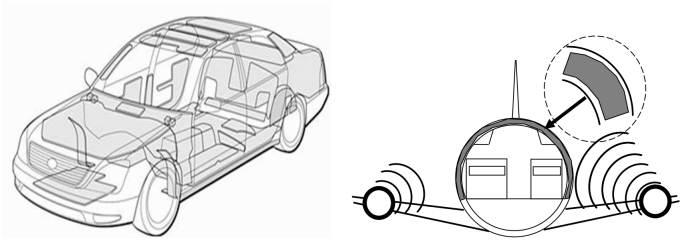

(a) (b)

Figure 1.1: Porous materials in a) a car and b) an airplane

Porous material has been widely used in various industrial fields for heat insulation, filtration, and acoustic absorption. Acoustic absorption is achieved by dissipating acoustic energy through the interactions between the particles of the solid and fluid components [1]. Acoustic liners, made from porous materials, are extensively utilized in vehicle design (Fig. 1.1), because they are cheap, lightweighted, and, as a result of the progress in technology and the focus on sustain-

ability, some of them are also recyclable [2]. In the car industry, the comfort of drivers and passengers has become more and more relevant to offer a better driving experience. The acoustic liner is capable of mitigating noise pollution, thereby contributing to the health, safety, and comfort of individuals exposed to sounds from both external surroundings and within the vehicle. In the European Union trains are the primary means of transportation for short and medium distances, so it is crucial to guarantee acoustic comfort during the trip [3]. Because of their lightweight properties, porous materials are also used in airplanes to reduce the transmission of engine noise to the cabin [1].

The porous materials for acoustic absorption are also found in the construction industry. In offices, schools, and houses, large open spaces are preferred to thigh spaces, both for the function they are going to perform (like large rooms for students) and for aesthetics [4]. Such spaces have high acoustic requirements, and the materials are chosen to fulfill those conditions.
In particular, to reduce the problem of engine noise, porous structures called acoustic liners, are used. [5] [6] [7].

1.2 Literature Review

A porous medium is a material that contains voids or pores. It is formed by two phases, a solid matrix and a void space, filled by one or more fluids [8]. The medium can be consolidated, meaning that the fluid passes through internal pores of the solid body, or unconsolidated, where the grains are not connected to each other and the fluid flows around them [9].

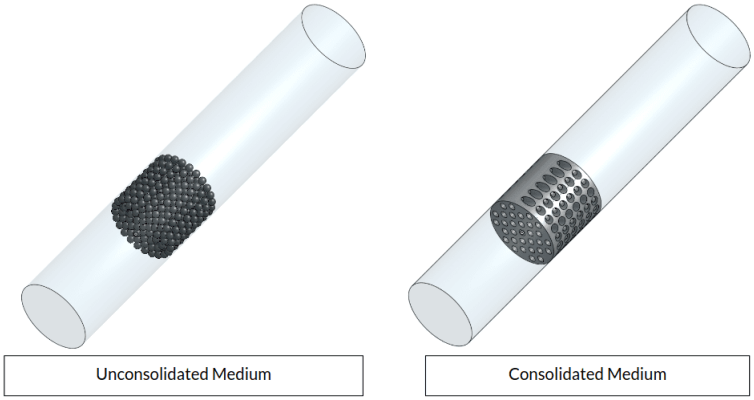

Figure 1.2: Schematic view of an unconsolidated and a consolidated media

The most significant propriety of this type of material is its porosity: in general, the higher the porosity, the easier is for the medium to be permeated [9]. Porosity is defined as the fraction of volume occupied by the fluid within the

porous material (the volume of pores) over the total volume and it is usually expressed as a percentage [10].

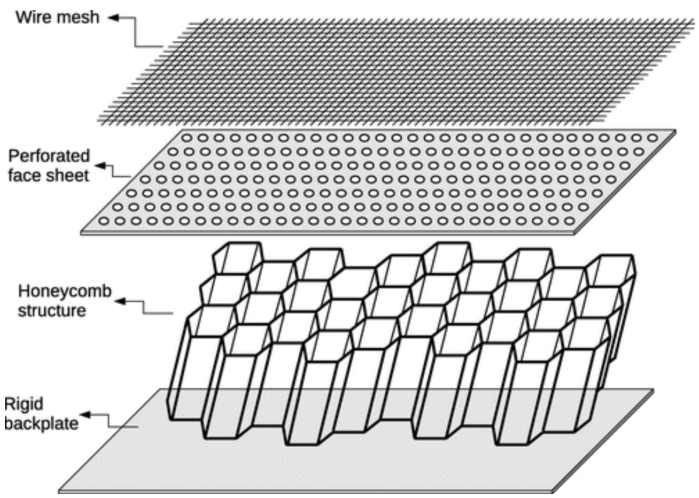

Figure 1.3: A layer-structured honeycomb acoustic liner

Acoustic liners are employed to reduce noise in different situations because they absorb or reflect sound waves to decrease noise levels, so they can create a quieter and more comfortable environment. The materials used could be foams, fibrous materials, and perforated metal sheets and they do not add significant weight.

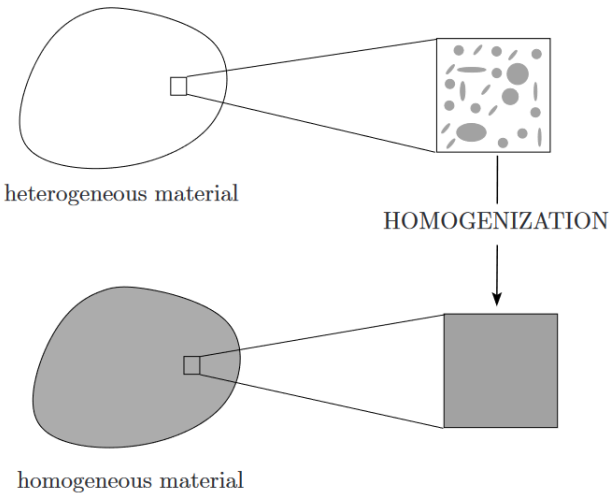

Figure 1.4: Homogenization of a heterogeneous material

A porous material is characterized by two length scales: a macroscopic length scale characterizing the global dimension, and a microscopic length scale charac-

terizing the microstructure of the pores. A layer-structured acoustic liner containing a honeycomb-shaped microstructure is shown in Fig. 1.3. The homogenization method is used to study the physical properties of such material [11]. Homogenization is an upscaling technique that allows the use of a macroscopic model to describe the global behavior of a given microstructured homogeneous or heterogeneous media (Fig. 1.4) [12] [13] [14].

1.3 Objectives

In this thesis, we aim to exploit the homogenization method to study the behavior of acoustic waves propagating through a prototypical acoustic liner: arrays of rigid cylindrical scatterers. The structure of the thesis is as follows: An introduction of the application of acoustic liners and the state of the art are summarized in chapter 1. In chapter 2, the acoustic wave equation is derived from the mass, momentum, and energy conservation equations (Linearized Navier-Stokes Equations); a non-dimensional mathematical model describing the macroscopic behavior of the acoustic liner is developed using the homogenization method. In chapter 3, two types of cylindrical microstructures are studied: the circular cylinder, and rectangular cylinders. The closure problem in the unit cell is solved to calculate the effective coefficients. The effectiveness of the obtained model will be validated with the full-geometry simulation of the material studied with COMSOL Multiphysics ® v.6.0. Finally, a summary of the work will be given in the last chapter.

Chapter 2

The Mathematical Model

2.1 The Acoustic Wave Equation

Sound is essentially a pressure wave. To describe how acoustic waves propagate in a fluid phase, we start with the laws of mass, momentum, and energy conservation. [15]. The mass source and external force are considered to be zero.
Mass conservation:

$$\frac{\partial \rho}{\partial t} + \frac{\partial}{\partial x_i}(\rho v_i) = 0, \tag{2.1}$$

where ρ is the fluid density and v_i is the flow velocity.
Momentum conservation:

$$\frac{\partial}{\partial t}(\rho v_i) + \frac{\partial}{\partial x_j}(P_{ij} + \rho v_j v_i) = 0, \tag{2.2}$$

where P_{ij} is the fluid stress vector.
Energy conservation:

$$\frac{\partial}{\partial t}\rho(e + \frac{1}{2}v^2) + \frac{\partial}{\partial x_i}(\rho v_i(e + \frac{1}{2}v^2)) = -\frac{\partial q_i}{\partial x_i} - \frac{\partial}{\partial x_i}(p v_i) + \frac{\partial}{\partial x_i}(\tau_{ij} v_j), \tag{2.3}$$

where e is the specific internal energy (internal energy per unit of mass), q_i is the heat flux and τ_{ij} is the viscous stress tensor.
Expanding Eq. (2.2)

$$v_i\left(\frac{\partial \rho}{\partial t} + \rho\frac{\partial v_j}{\partial x_j} + \frac{\partial \rho}{\partial x_j}v_j\right) + \rho\frac{\partial v_i}{\partial t} + \frac{\partial P_{ij}}{\partial x_j} + \rho v_j\frac{\partial v_i}{\partial x_j} = 0, \tag{2.4}$$

and combing with Eq. (2.1), there is

$$\rho\frac{\partial v_i}{\partial t} + \frac{\partial P_{ij}}{\partial x_j} + \rho v_j\frac{\partial v_i}{\partial x_j} = 0. \tag{2.5}$$

The fluid stress tensor P_{ij} can be written as

$$P_{ij} = p\delta_{ij} - \tau_{ij}, \tag{2.6}$$

where δ_{ij} is the unit tensor. τ_{ij} can be neglected here

$$P_{ij} = p\delta_{ij}. \tag{2.7}$$

From Eq. (2.4), the following equation is obtained:

$$\rho(\frac{\partial v_i}{\partial t} + v_j\frac{\partial v_i}{\partial x_j}) + \frac{\partial p}{\partial x_j} = 0 \tag{2.8}$$

Now the focus is on equation (2.1). The *product rule* is applied

$$\frac{\partial}{\partial x_i}(fg_i) = f\frac{\partial g_i}{\partial x_i} + \frac{\partial f}{\partial x_i}g_i \tag{2.9}$$

resulting in

$$\frac{\partial \rho}{\partial t} + \rho\frac{\partial v_i}{\partial x_i} + \frac{\partial \rho}{\partial x_i}v_i = 0 \tag{2.10}$$

Considering the fluid to be stagnant and uniform, and writing the density and velocity as a mean value and a fluctuation part, $\rho = \bar{\rho} + \rho'$ and $v = \bar{v} + v'$ with $\bar{v} = 0$ (the fluid is stagnant), Eq. (2.10) now becomes:

$$\frac{\partial \bar{\rho}}{\partial t} + \frac{\partial \rho'}{\partial t} + (\bar{\rho} + \rho')\frac{\partial v_i'}{\partial x_i} + \frac{\partial}{\partial x_i}(\bar{\rho} + \rho')v_i' = 0. \tag{2.11}$$

Since the fluid is considered to be uniform, the mean density $\bar{\rho} = \rho_0$ is a constant. Hence,

$$\frac{\partial \rho'}{\partial t} + \rho_0\frac{\partial v_i'}{\partial x_i} + \rho'\frac{\partial v_i'}{\partial x_i} + \frac{\partial \rho'}{\partial x_i}v_i' = 0. \tag{2.12}$$

Neglecting the second-order terms, the linearized form of Eq. (2.10) is

$$\frac{\partial \rho'}{\partial t} + \rho_0\frac{\partial v_i'}{\partial x_i} = 0 \tag{2.13}$$

Applying linearization for Eq. (2.8), resulting in (considering $p = \bar{p} + p'$):

$$\begin{aligned}(\rho_0 + \rho')(\frac{\partial v_i'}{\partial t} + v_j'\frac{\partial v_i'}{\partial x_j}) + \frac{\partial p'}{\partial x_j} = 0\\ \rho_0\frac{\partial v'}{\partial t} + \frac{\partial p'}{\partial x_j} = 0\end{aligned} \tag{2.14}$$

Applying time derivative for Eq. (2.13) and divergence for Eq. (2.14), there are

$$\frac{\partial^2 \rho'}{\partial t^2} + \frac{\partial}{\partial t}(\rho_0\frac{\partial v_i'}{\partial x_i}) = 0 \tag{2.15}$$

$$\frac{\partial}{\partial x_i}(\rho_0 \frac{\partial v_i'}{\partial t}) + \frac{\partial^2 p'}{\partial x_i \partial x_j} = 0 \tag{2.16}$$

Subtracting Eq. (2.15) from Eq. (2.16) leads to

$$\frac{\partial^2 \rho'}{\partial t^2} - \frac{\partial^2 p'}{\partial x_i \partial x_j} = 0. \tag{2.17}$$

Furthermore, we use the isentropic condition $p' = c_0^2 \rho'$ (c_0 is the speed of sound) to rewrite p' and apply the Fourier transform with $\hat{p}e^{-i\omega t}$ convention (ω is the complex frequency), to get the wave equation in the frequency domain,

$$\frac{1}{c_0^2}(-i\omega)^2 \hat{p}e^{-i\omega t} - \frac{\partial^2 \hat{p}e^{-i\omega t}}{\partial x_i \partial x_j} = 0. \tag{2.18}$$

The division by $-e^{-i\omega t}$ brings to the *acoustic wave equation*, also known as the Helmholtz equation

$$\frac{\partial^2 \hat{p}}{\partial x_i \partial x_j} + k^2 \hat{p} = 0, \tag{2.19}$$

where $k = \dfrac{\omega}{c_0}$ is the wave number.

2.2 Homogenization Method

The problem of the interaction between a fluid and an array of rigid cylinders is now approached using the up-scaling technique, meaning that a macroscopic model is obtained starting from the study of the microscopic behavior. [11] [12]

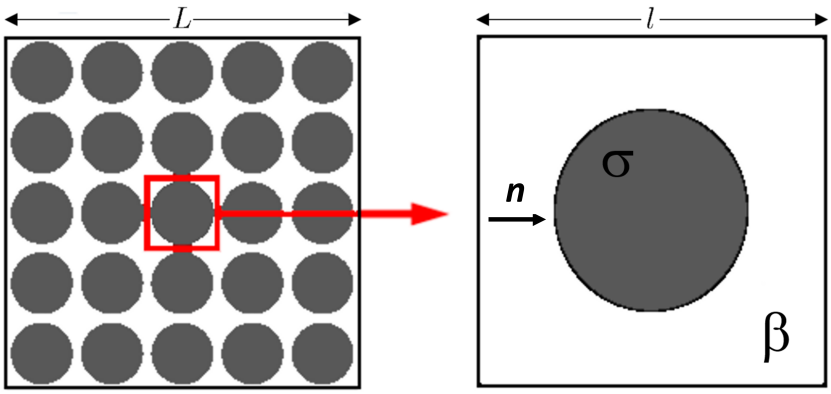

Figure 2.1: β fluid phase (air) and σ solid phase

The length of the matrix is characterized by the parameter L, while the unit cell studied is l long. Ω is the area of the unit cell and Ω_f is the area of the fluid in the unit cell; γ_s is the solid boundary while $\delta\Omega$ is both γ_s and the boundary of the cell.

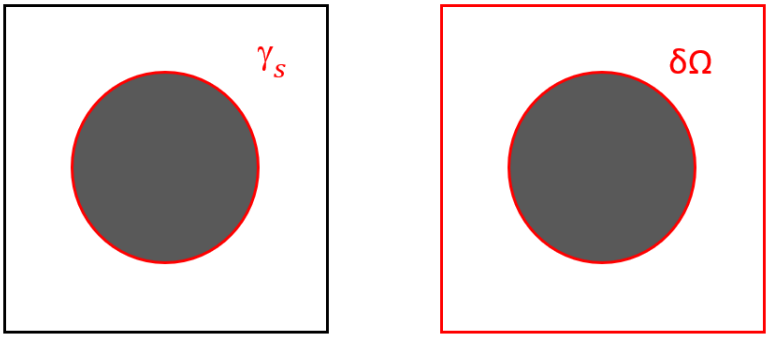

Figure 2.2: visual representation of γ_s and $\delta\Omega$

If $\boldsymbol{r}$ is used for general coordinates, $\boldsymbol{x}$ for the macroscopic ones and $\boldsymbol{y}$ for the microscopic, the following relationship is true:

$$\frac{\partial}{\partial r_i^*} = \epsilon \frac{\partial}{\partial x_i^*} + \frac{\partial}{\partial y_i^*}. \tag{2.20}$$

therefore, the acoustic wave equation obtained in the previous paragraph becomes:

$$\frac{\partial^2 p}{\partial r_i^2} + k^2 p = 0 \tag{2.21}$$

in β-phase (the fluid only goes through air). Also, the condition of perfectly rigid solid interface leads to:

$$\frac{\partial p}{\partial r_i} n_i = 0 \tag{2.22}$$

at γ_s. n_i is the normal vector on γ_s pointing outwards the fluid phase 2.1.

New variables are introduced to get a nondimensionalized of the Eq. (2.21) and (2.22).

$$p^* = \frac{p}{\Delta p_{ref}},\ \ c^* = \frac{c}{c_{ref}},\ \ \omega^* = \frac{\omega L}{c_{ref}},\ \ k^* = \frac{\omega L}{c},\ \ r_i^* = \frac{r_i}{l},\ \ \epsilon = \frac{l}{L}$$

The superscripts $*$ represents dimensionless variables.
Noted that $k = \dfrac{\omega}{c_0}$, the variables just defined can be substituted inside the previous equations, therefore:

$$\frac{\partial^2 p^*}{\partial r_i^{*2}} + \epsilon^2 k^{*2} p^* = 0,\ \text{in } \beta\text{-phase} \tag{2.23}$$

$$\frac{\partial p^*}{\partial r_i^*} n_i = 0,\ \text{at } \gamma_s \tag{2.24}$$

2.2.1 Different Orders of the Problem

Now, p^* is manipulated through the power series expansion to get to different orders of ϵ^n

$$p^* = p_0^* + \epsilon p_1^* + \epsilon^2 p_2^* + \mathcal{O}(\epsilon^3) \tag{2.25}$$

Orders higher than $\mathcal{O}(\epsilon^3)$ can be neglected. The focus is on orders $\mathcal{O}(\epsilon^0)$, $\mathcal{O}(\epsilon^1)$ and $\mathcal{O}(\epsilon^2)$.

$$(\epsilon\frac{\partial}{\partial x_i^*} + \frac{\partial}{\partial y_i^*})^2(p_0^* + \epsilon p_1^* + \epsilon^2 p_2^*) + \epsilon^2 k^{*2}(p_0^* + \epsilon p_1^* + \epsilon^2 p_2^*) = 0,\ \text{in } \beta\text{-phase} \tag{2.26}$$

$$(\epsilon\frac{\partial}{\partial x_i^*} + \frac{\partial}{\partial y_i^*})(p_0^* + \epsilon p_1^* + \epsilon^2 p_2^*) n_i = 0,\ \text{at } \gamma_s \tag{2.27}$$

- ϵ^0 **order**:
In β-phase

$$\frac{\partial^2 p_0^*}{\partial y_i^{*2}} = 0 \tag{2.28}$$

therefore

$$p_0^* = p_0^*(\mathbf{x}) \tag{2.29}$$

At γ_s

$$\frac{\partial p_0^*}{\partial y_i^*} n_i = 0 \tag{2.30}$$

- ϵ^1 **order:**
In β-phase

$$\begin{aligned} (2\epsilon \frac{\partial^2}{\partial x_i^* y_i^*} + \frac{\partial^2}{\partial y_i^{*2}})(p_0^* + \epsilon p_1^*) = 0 \\ 2\frac{\partial^2 p_0^*}{\partial x_i^* y_i^*} + \frac{\partial^2 p_1^*}{\partial y_i^{*2}} = 0 \end{aligned} \tag{2.31}$$

From the equations just obtained for ϵ^0 order, it is evident the independence of p_0 from the microscopic coordinate $\mathbf{y}$, meaning that p_0^* is only found in the macroscopic model. The simplified equation is

$$\frac{\partial^2 p_1^*}{\partial y_i^{*2}} = 0 \tag{2.32}$$

At γ_s

$$(\frac{\partial p_0^*}{\partial x_i^*} + \frac{\partial p_1^*}{\partial y_i^*}) n_i = 0 \tag{2.33}$$

Now only p_1^* has to be defined. A new vector, $\mathbf{s}^*$, is introduced, so that

$$p_1^* = -s_i^* \frac{\partial p_0^*}{\partial x_i^*} \tag{2.34}$$

The combination of Eq. (2.32) and the definition of $\boldsymbol{s^*}$ brings to

$$\frac{\partial^2 s_j^*}{\partial y_i^{*2}} = 0 \text{ in } \beta\text{-phase} \tag{2.35}$$

and using (2.33) the equation becomes:

$$n_i(\delta_{ij} - \frac{\partial}{\partial y_i^*} s_j^*) = 0 \text{ at } \gamma_s \tag{2.36}$$

To compute s_i^*, more conditions to close the problem are needed. The two conditions come from the definition of the unit cell, that is l_i-periodic, where l_i is its length, and s_i depends only on macroscopic coordinates (2.34), therefore:

$$s_j^*(r + l_i) = s_j^*(r) \text{ periodic condition} \tag{2.37}$$

and

$$\langle \boldsymbol{s^*} \rangle = \frac{1}{\Omega_f} \iint_{\Omega_f} s_j^* dA = 0 \text{ average constraint} \tag{2.38}$$

where Ω is the area of the unit cell.
From equation
- ϵ^2 order:
In β-phase

$$\begin{aligned} (\epsilon^2 \frac{\partial^2}{\partial x_i^{*2}} + 2\epsilon \frac{\partial^2}{\partial x_i^* y_i^*} + \frac{\partial^2}{\partial y_i^{*2}})(p_0^* + \epsilon p_1^* + \epsilon^2 p_2^*) + \epsilon^2 k^{*2} p_0^* = 0 \\ \frac{\partial^2 p_0^*}{\partial x_i^{*2}} + 2\frac{\partial^2 p_1^*}{\partial x_i^* y_i^*} + \frac{\partial^2 p_2^*}{\partial y_i^{*2}} + k^{*2} p_0^* = 0 \end{aligned} \tag{2.39}$$

At γ_s

$$(\frac{\partial p_1^*}{\partial x_i^*} + \frac{\partial p_2^*}{\partial y_i^*}) n_i = 0 \tag{2.40}$$

Now the averaging operator is introduced for the term $\frac{\partial^2 p_2^*}{\partial y_i^{*2}}$. This will lead to obtain, after a few calculations, a macroscopic model.

$$I = \frac{1}{\Omega_f} \iint_{\Omega_f} (p_0^* \frac{\partial^2 p_2^*}{\partial y_i^{*2}}) dA \tag{2.41}$$

Green's formula is used to get

$$\iint_{\Omega_f} p_0^* \frac{\partial^2 p_2^*}{\partial y_i^{*2}} dA = \int_{\delta\Omega} p_0^* n_i \frac{\partial p_2^*}{\partial y_i^*} ds \tag{2.42}$$

The union of equation (2.40) and (2.34) brings to

$$n_i \frac{\partial p_2^*}{\partial y_i^*} = -n_i \frac{\partial p_1^*}{\partial x_i^*} = n_i s_j^* \frac{\partial^2 p_0^*}{\partial x_i^* x_j^*} \tag{2.43}$$

The term $\nabla_{\mathbf{y}}^2 p_2^*$ can be rewritten using (2.39) and the index notation as:

$$\frac{\partial^2 p_2^*}{\partial y_i^{*2}} = -(2\frac{\partial}{\partial x_i}(\frac{\partial p_1^*}{\partial y_i^*}) + \frac{\partial^2 p_0^*}{\partial x_i^{*2}} + k^{*2} p_0^*) \tag{2.44}$$

Substituting the results of Eq. (2.43) and Eq. (2.44) and using Eq. (2.34), knowing that s_i^* is independent of x_i^*, the equation (2.42) becomes:

$$\iint_{\Omega_f} p_0^* (2\frac{\partial}{\partial x_i^*}(\frac{\partial s_j^*}{\partial y_i^*} \frac{\partial p_0^*}{\partial x_j^*}) - \frac{\partial^2 p_0^*}{\partial x_i^{*2}} - k^{*2} p_0^*) dA = \int_{\delta\Omega} p_0^* n_i s_j^* \frac{\partial^2 p_0^*}{\partial x_i^* x_j^*} ds \tag{2.45}$$

Using the averaging operator for each term of equation (2.45), the *effective medium equation* is found:

$$\beta_{ij}\frac{\partial^2 p_0^*}{\partial x_i^* x_j^*} + \frac{1}{\Omega_f}\iint_{\Omega_f} k^{*2} p_0^* dA = 0 \tag{2.46}$$

where

$$\beta_{ij} = \frac{1}{\Omega_f}\left(\int_{\gamma_s} n_i s_j^* ds + \iint_{\Omega_f} (\delta_{ij} - 2\frac{\partial s_j^*}{\partial y_i^*})\right) dA \tag{2.47}$$

and

$$\frac{1}{\Omega_f}\iint_{\Omega_f} k^{*2} p_0^* dA = k^{*2} p_0^* \tag{2.48}$$

To rewrite the first term of equation (2.47) (2.35) is integrated in the fluid domain, multiplied by s_k^*

$$\iint_{\Omega_f} s_k^* \frac{\partial^2 s_j^*}{\partial y_i^{*2}} dA = \iint_{\Omega_f} \frac{\partial}{\partial y_i^*}(s_k^* \frac{\partial s_j^*}{\partial y_i^*}) dA - \iint_{\Omega_f} \frac{\partial s_k^*}{\partial y_i^*}\frac{\partial s_j^*}{\partial y_i^*} dA = 0 \tag{2.49}$$

using *Green's formula* for $\iint_{\Omega_f} \frac{\partial}{\partial y_i^*}(s_k^* \frac{\partial s_j^*}{\partial y_i^*}) dA$:

$$\int_{\delta\Omega} s_k^* \frac{\partial s_j^*}{\partial y_i^*} n_i ds - \iint_{\Omega_f} \frac{\partial s_k^*}{\partial y_i^*}\frac{\partial s_j^*}{\partial y_i^*} dA = \tag{2.50}$$

The integral is null for the boundaries of the unit cell, so now

$$\int_{\gamma_s} s_k^* n_j ds = \iint_{\Omega_f} \frac{\partial s_k^*}{\partial y_i^*}\frac{\partial s_j^*}{\partial y_i^*} dA \tag{2.51}$$

knowing that $n_j = \frac{\partial s_j^*}{\partial y_i^*} n_i$. Changing indices the previous equation can be rewritten as:

$$\int_{\gamma_s} s_j^* n_i ds = \iint_{\Omega_f} \frac{\partial s_j^*}{\partial y_k^*}\frac{\partial s_i^*}{\partial y_k^*} dA \tag{2.52}$$

Now β_{ij} is

$$\beta_{ij} = \frac{1}{\Omega_f}\iint_{\Omega_f} (\frac{\partial s_j^*}{\partial y_k^*}\frac{\partial s_i^*}{\partial y_k^*} + \delta_{ij} - 2\frac{\partial s_j^*}{\partial y_i^*}) dA \tag{2.53}$$

Equation (2.46) can be written using only macroscopic coordinates as:

$$\beta_{ij}\frac{\partial^2 p_0^*}{\partial x_i^* x_j^*} + k^{*2} p_0^* = 0 \tag{2.54}$$

where β_{ij}, for the isotropic case, is $\beta_{ij} = \beta\delta_{ij}$.
In the next chapter, β_{ij} is calculated both for isotropic and non-isotropic case.

Chapter 3

Results and Discussion

The first step in solving the effective medium equation (2.54) is to calculate the components of the tensor β_{ij}. This involves using COMSOL Multiphysics ® to solve the closure variable in a unit cell. We calculate for the isotropic case, a circular cylinder, and the non-isotropic one, a rectangular cylinder. The results reveal how the values of these components change to the porosity, plotting for each case a graph and adding the corresponding polynomial fitting. Once the equations are obtained, they are applied to the full geometry. The comparison between the results given by the general equation (2.21) to describe a matrix of rigid cylinders and the ones given by the equivalent effective medium equation demonstrates whether the approximation is valid. The same procedure is followed to test the effective medium equation for an array of rectangular prisms, using the data obtained from the non-isotropic case.

3.1 Unit cell solutions

3.1.1 Isotropic case: cylinder scatterers

The first case is a cylinder with radius R inside a square whose side is 1. The radius is related to the porosity ϕ by the formula $R = \sqrt{\frac{(1-\phi)}{\pi}}$, so when the porosity grows, the cylinder gets smaller. The porosity goes from 0.3 to 0.9 with a step of 0.1.
β_{ij} is a function of s_i^*, so s_1^* and s_2^* are calculated, recalling the boundary conditions imposed (2.37) (2.38).

The following figures show the values of s_1^* and s_2^*, respectively:

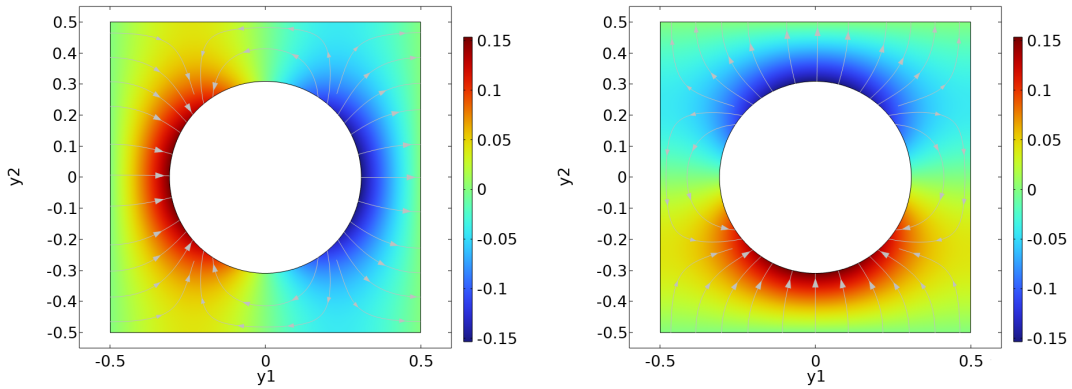

(a) s_1^* (b) s_2^*

Figure 3.1: visual representation of s_i^* for a cylinder, $\phi = 0.7$

Figure 3.1(a) is equal to figure 3.1(b) but with a rotation of 90°. The flux lines go from the areas with a lower concentration to the ones with a higher one. Figure 3.1(a) is symmetric to the y_1 axis, figure 3.1(b) to y_2.

3.1.2 Non-isotropic case: rectangle scatterers

In the second case, a rectangle that is $3z$ long and $2z$ wide (ratio between the width and the length λ here is $\lambda_1 = 3:2$) is analyzed, where z is a function of ϕ given by the formula $z = \sqrt{\frac{(1-\phi)}{6}}$. The porosity in this problem goes from 0.5 to 0.9, 0.1 step. The square side is again 1. s_1^* and s_2^* are defined in the same way as the ones written for the first case. The corresponding visual representation is obtained using COMSOL Multiphysics ®:

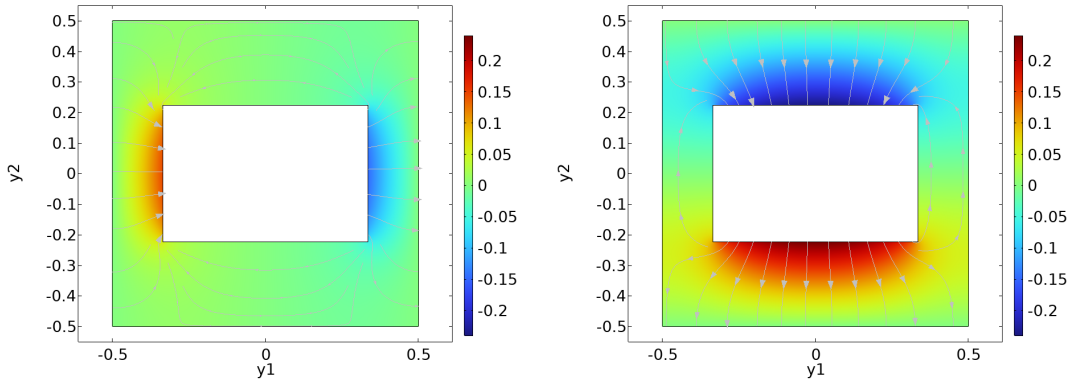

(a) s_1^* (b) s_2^*

Figure 3.2: visual representation of s_i^* for a rectangle, $\phi = 0.7$

Once more, 3.2(a) is 3.2(b) rotated by 90° and the flux lines move from lower to higher concentration, but now the intensity is different: the values for 3.2(b) are lower in the area where the flux lines enter, and higher where they exit in comparison to 3.2(a).

Different Aspect Ratio

The shape of rectangle scatterers is characterized by the aspect ratio,λ, which is defined as the length-to-width ratio. In this section, the closure problem of s_i^* is solved for different aspect ratios. Corresponding model coefficients β_{11} and β_{22} are evaluated for different aspect ratios and different porosity. Fig. 3.3 and Fig. 3.4 show the field of s_i^* for $\phi = 0.7$, and the aspect ratios $\lambda_2 = 6:5$ and $\lambda_3 = 1:0.2$.

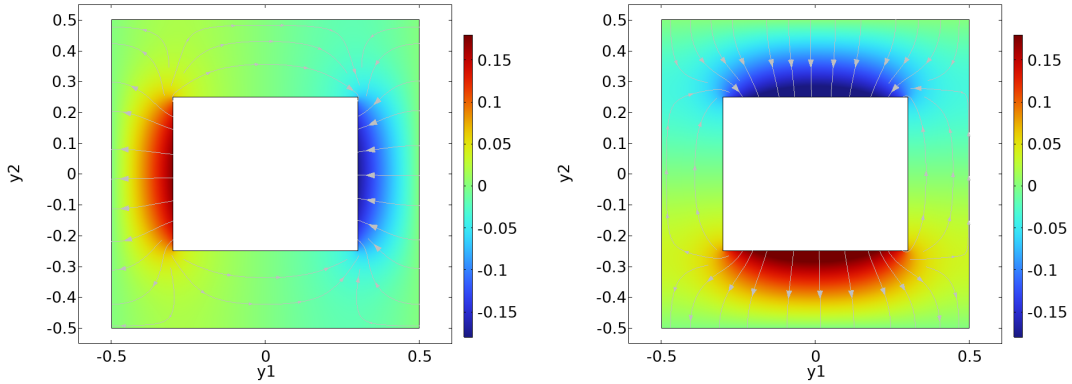

(a) s_1^* (b) s_2^*

Figure 3.3: $\lambda_2 = 6:5$

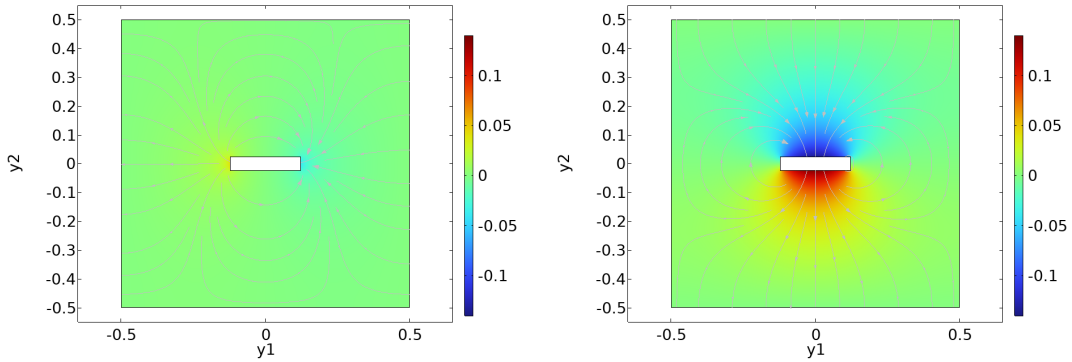

(a) s_1^* (b) s_2^*

Figure 3.4: $\lambda_2 = 1:0.2$

In figure both figures, as in figure 3.2, for s_2^* the colors are more intense, meaning that the values are higher or lower than for s_1^*. The most evident difference is in figure 3.4, where s_1^* is almost constant throughout β-phase, while s_2^* has more significant concentration, that is anyway still closer to zero than in 3.2 and 3.3. This could be due to the fact that the rectangle is smaller for λ_3, so there is less interference between the fluid and the solid.

3.2 Components of β_{ij}

3.2.1 Isotropic case

The data that the program has calculated for β_{11}, β_{22}, β_{12} and β_{21} are now plotted:

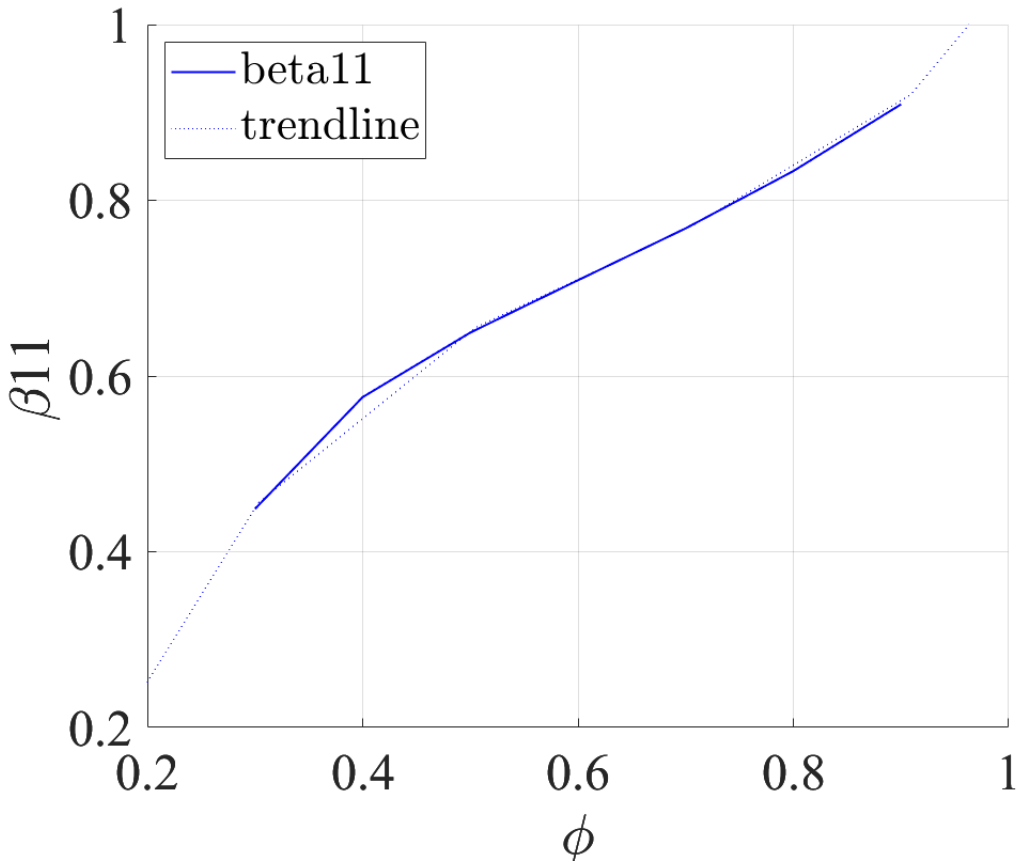

Figure 3.5: correlation between ϕ and β_{11} (or β_{22}) and its polynomial fitting function

β_{11} and β_{22} have the same values only graph is sufficient; β_{12} and β_{21} are almost zero and can be neglected. In the graph, a linear correlation between ϕ and β_{11} (or β_{22}) is evident and it can be approximated by an increasing cubic function: $\beta_{11} = 2.3474\phi^3 - 4.5812\phi^2 + 3.5175\phi - 0.2549$.

3.2.2 Non-isotropic case

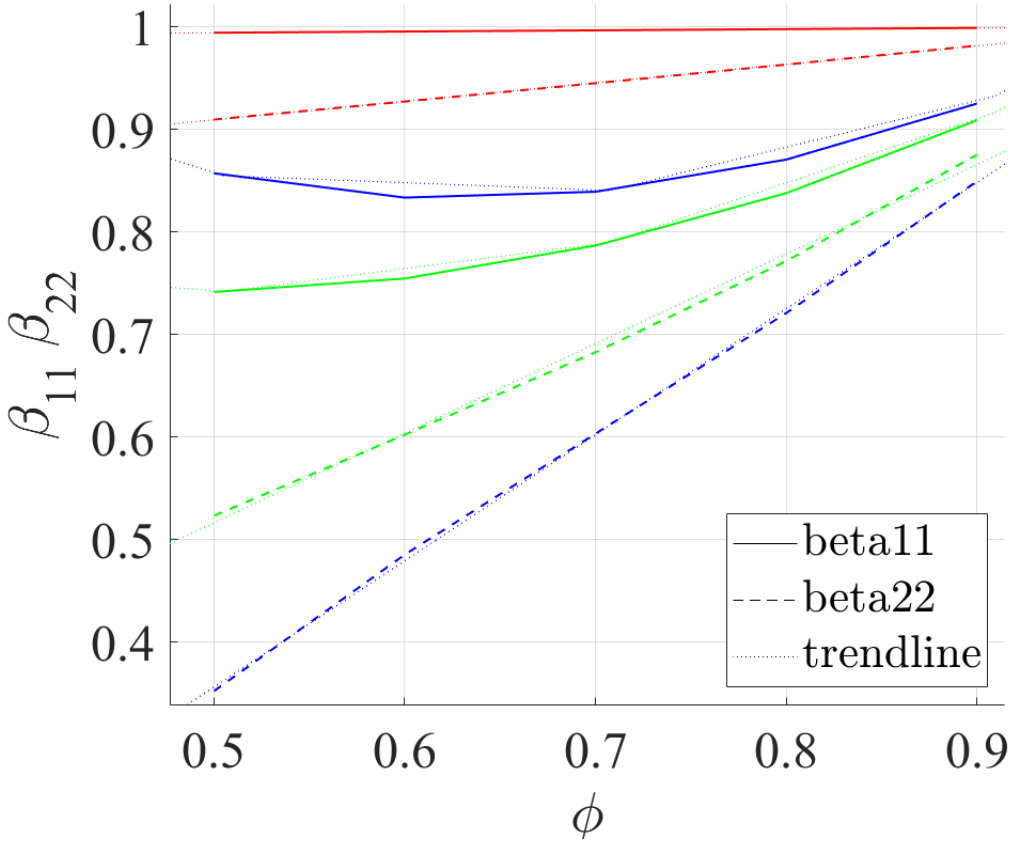

Figure 3.6: blue) λ_1, green) λ_2, red) λ_3

The off-diagonal components β_{12} and β_{21} are zeros for all the λ, and we show in Fig. 3.6 the dependence of β_{11} and β_{22} on porosity for different aspect ratios. For β_{11} the higher the ratio, the flatter the curve: for λ_1 and λ_2 it can be approximated to a parabola (the function for λ_2 has a lower vortex and has a higher slope than for λ_1), while for λ_3 it is a straight line, almost constant. β_{22}, meanwhile, is a straight line for all the cases, but now there is no direct correlation between λ and the slope of the lines: the most slope is given by the function for λ_1, the least for λ_3. The two functions for λ_3 are very similar to each other.

These are the functions obtained using a polynomial fitting:

Table 3.1: Polynomial fitting results of non-isotropic β_{11} and β_{22} for different aspect ratios.

	β_{11}	β_{22}
λ_1	$1.3023\phi^2 - 1.6501\phi + 1.3559$	$1.2299\phi - 0.2587$
λ_2	$0.9635\phi^2 - 0.9307\phi + 0.966$	$0.8734\phi + 0.0797$
λ_3	$0.0117\phi + 0.9884$	$0.1802\phi + 0.8191$

3.3 Numerical simulation

Now the approximation given by the effective medium equation (2.54) to the general one (2.19) is tested, to see whether the model built can be used or not. The general idea is to let the acoustic wave develop completely, so the changing of pressure throughout the matrix and the model can be measured more precisely, and compare the two different results. To achieve so, for both cases, two blocks are added, one before the matrix and one after. The first block has the same dimension u as the second one, the rectangle is $3u$ wide and u high. The general scheme is the following:

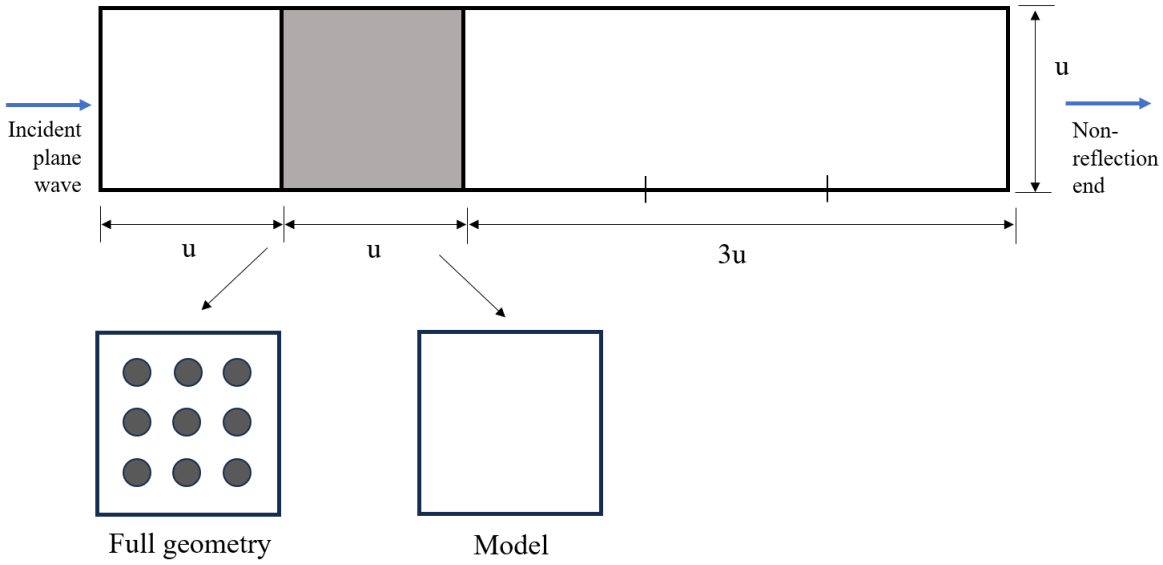

Figure 3.7: Schematic view of the computational domain

On the left side, the one that the acoustic wave hits first, the Dirichlet boundary condition is imposed, and the function is the incident plane wave equation of the pressure $p_0^{*\,-ikx}$ (incident because it hits the surface perpendicularly, plane wave because it has only one frequency given), where i is the imaginary unit, k is the wave number obtained using $f = 100Hz$ in this first example, then $f = 50Hz$ and $f = 200Hz$, and x indicates the position in the model.

On the right side, the wave goes out of the domain without reflection.
The assumption made is that there is no flux on the upper and lower sides.

3.3.1 Mesh

Matrix of rigid cylinders

The first problem computed is a matrix of rigid cylinders. The porosity is calculated using the formula $\phi = \dfrac{u^2 - n^2\pi R^2}{u^2} = 0.6783$, where u is the length of the square and n is the number of cylinders for each row (here it is 20).

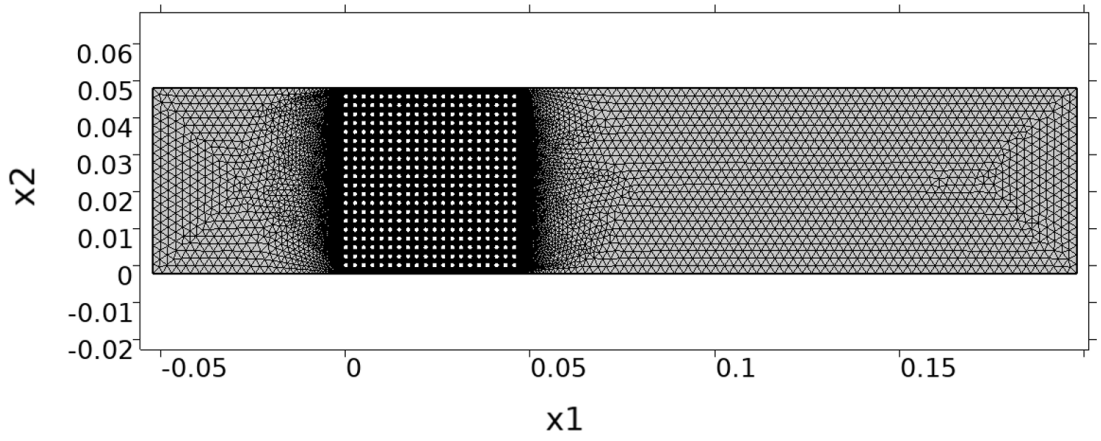

Figure 3.8: extremely fine mesh

Matrix of rectangular prisms

For this problem the same procedure as for a matrix of rigid cylinders is followed. The porosity is $\phi = \dfrac{u^2 - (ab)(cd)}{u^2} = 0.5811$, where a is the length of the rectangle used to plot the matrix and b is its width, c is the number of rectangles in $x1$ direction and d in $x2$.

The ratio here is λ_1.

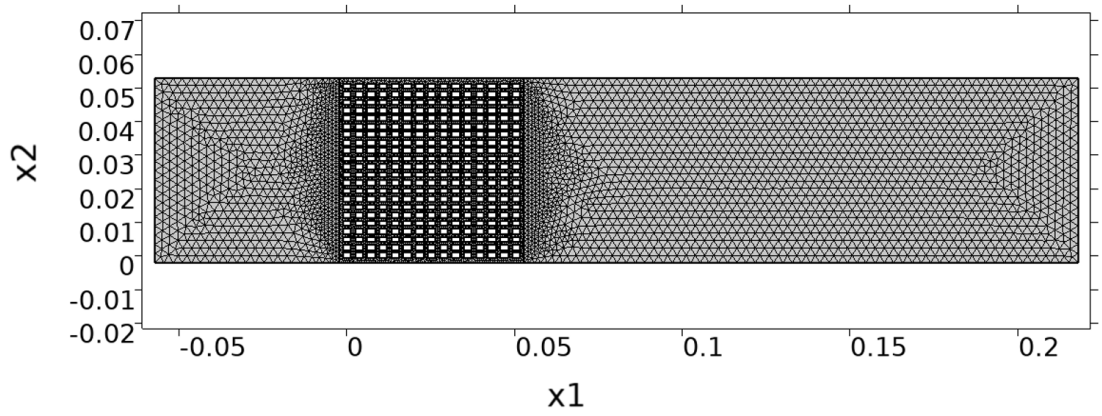

Figure 3.9: extremely fine mesh

Effective media

For the numerical simulations of acoustic waves transmitted through effective media, the derived macroscopic models with calculated coefficient β_{ij} for circular scatterers (3.2.1) and rectangular scatterers (3.1) are used.

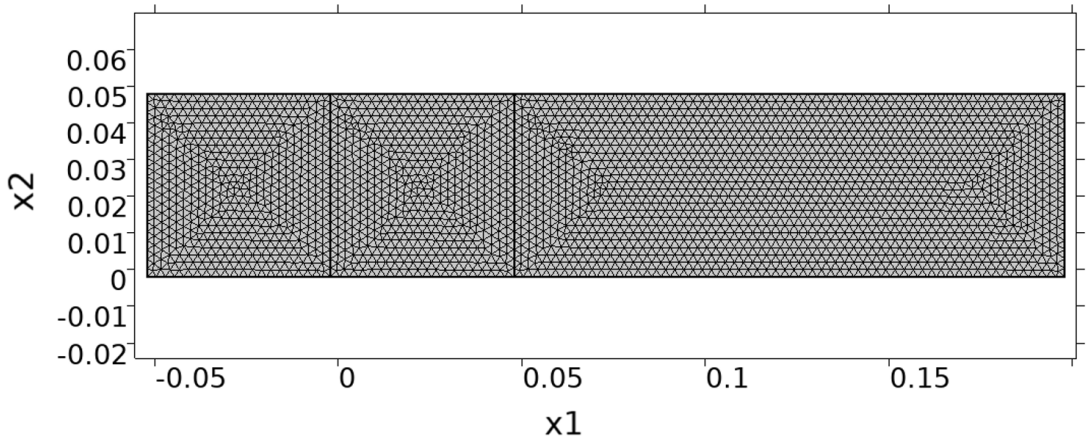

Figure 3.10: extremely fine mesh

The calculation of $\beta_{11}(\phi)$ and $\beta_{22}(\phi)$ are made substituting the ϕ given by the previous calculations: those β_{ij} are used in (2.54), that, for the isotropic case, can be rewritten as

$$\frac{\partial^2 p_0^*}{\partial x_i^* x_j^*} + k_{eff}^{*2} p_0^* = 0 \tag{3.1}$$

where $k^*_{eff} = \dfrac{k^*}{\sqrt{(\beta_{ij})}}$.
In the non-isotropic problem the tensor β_{ij} is diagonal, so two components need to be defined.

3.3.2 Simulation results

The acoustic wave $p_0^{*\,-ikx}$ can be divided into a real part p_r and an imaginary part p_i.
p_r for the different geometries for $f = 50Hz$ is:

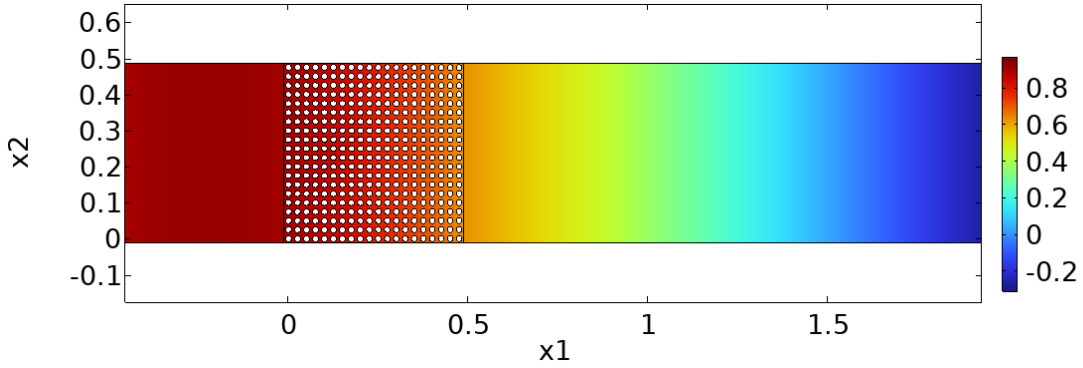

(a) full geometry

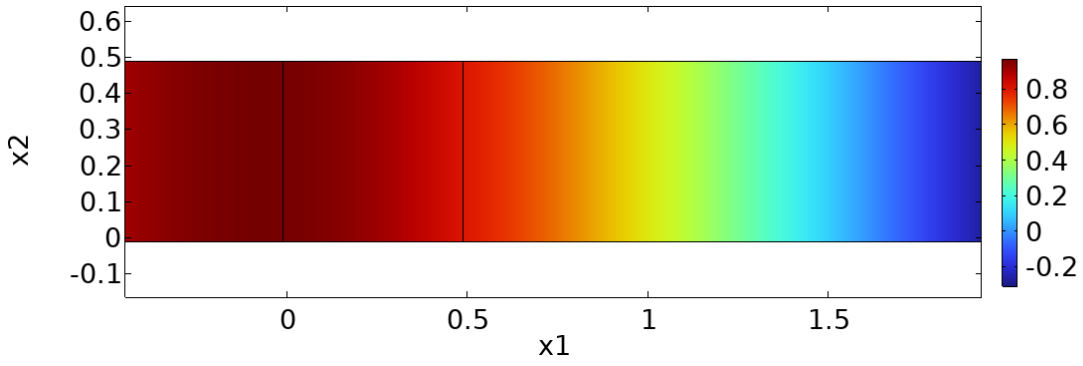

(b) effective medium

Figure 3.11: Matrix of rigid cylinders

As expected, the value of the p_r decreases when passing through the matrix, starting from a value of almost 1 Pa at the beginning of the scatterer region (the fact that the pressure at the beginning is not exactly 1 is due to the interface between the free field and the porous medium).

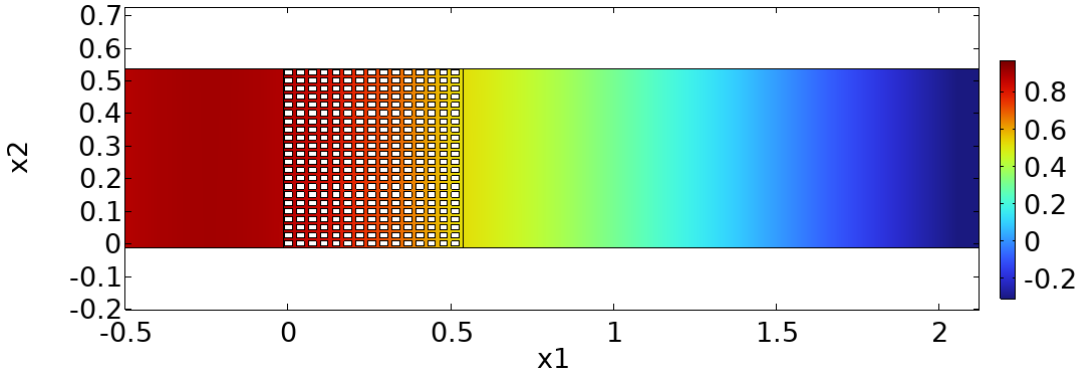

(a) full geometry

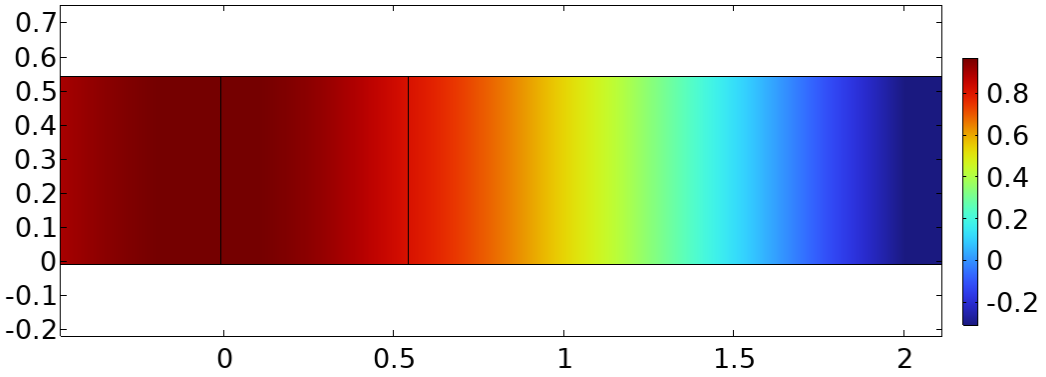

(b) effective medium

Figure 3.12: Matrix of rectangular prisms

For this case as well the observations just made are valid, but here even lower values in the final part of the model and higher at the beginning are reached, both for the matrix and the block.

The comparison between the imaginary parts of the wave is the following:

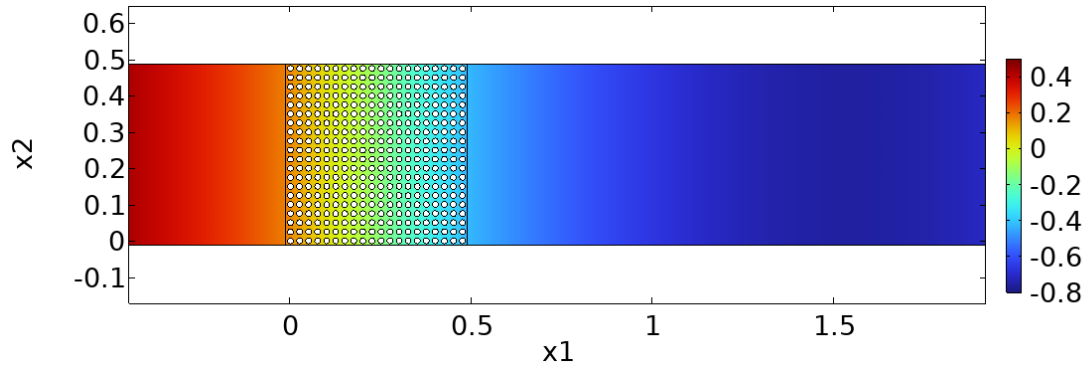

(a) full geometry

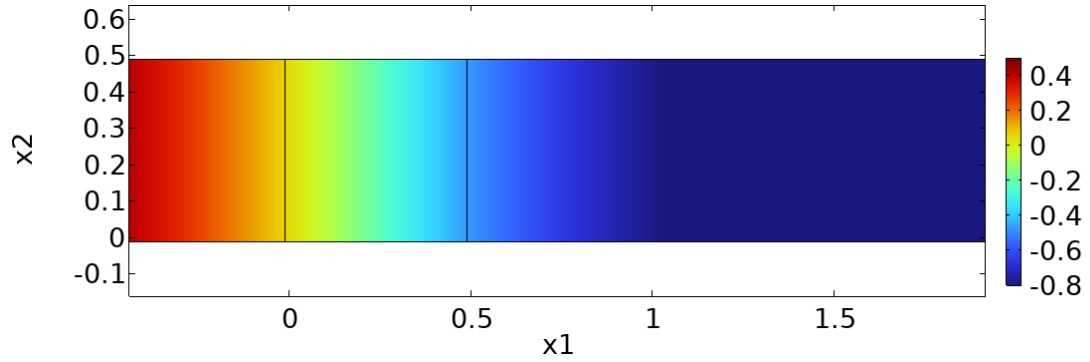

(b) effective medium

Figure 3.13: Matrix of rigid cylinders

For the imaginary part, the difference is even smaller than for the real part. Here, the values at the beginning are higher for the full geometry, and lower at the end for the effective medium.

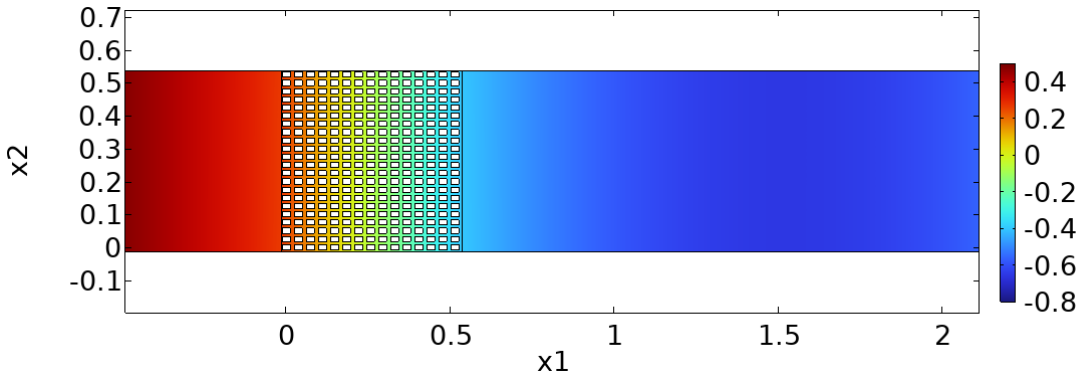

(a) full geometry

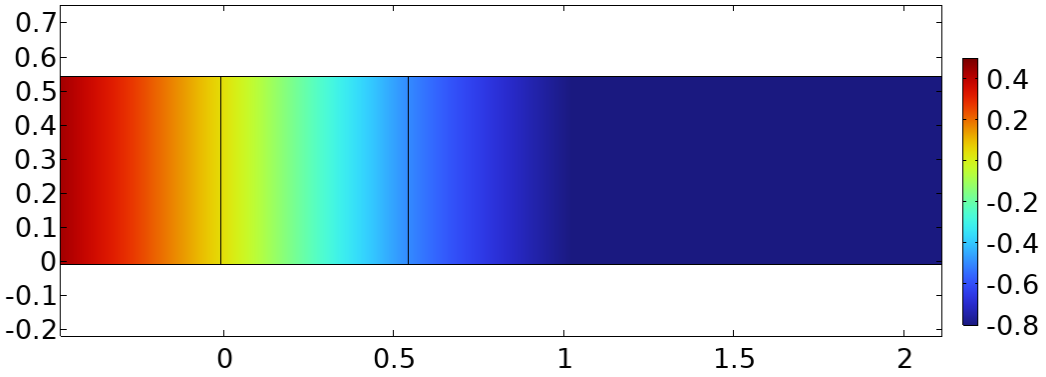

(b) effective medium

Figure 3.14: Matrix of rectangular prisms

Comparing figure 3.13 and 3.14, it is evident that the approximation is closer for the isotropic problem.
For all the cases, p_i becomes negative when the flux passes through the model and keeps decreasing.

Now $f = 100Hz$ is tested.

-p_r:

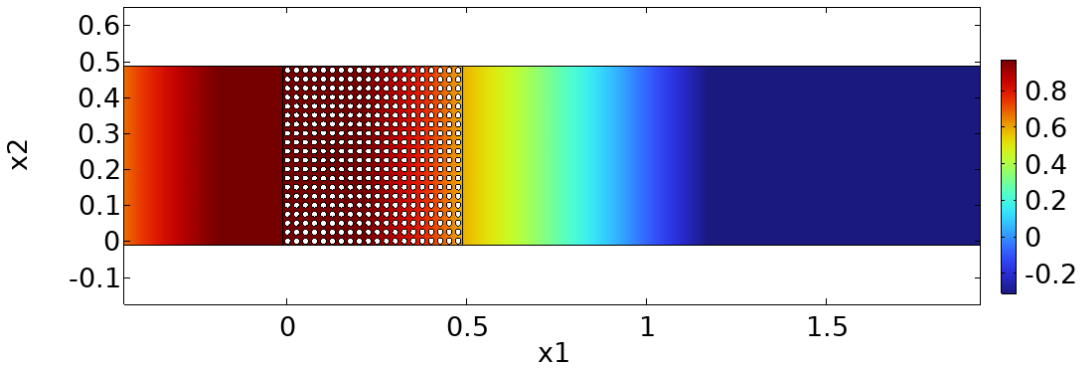

(a) full geometry

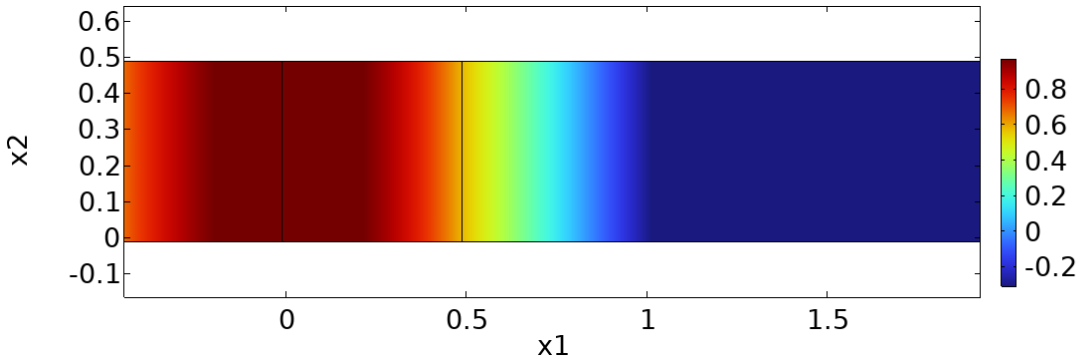

(b) effective medium

Figure 3.15: Matrix of rigid cylinders

For a higher frequency, i.e. a shorter wavelength, the sinusoidal behavior of the acoustic wave becomes visible: p_r grows until the beginning of the scatterer region, reaching values higher than 1, then it decreases.

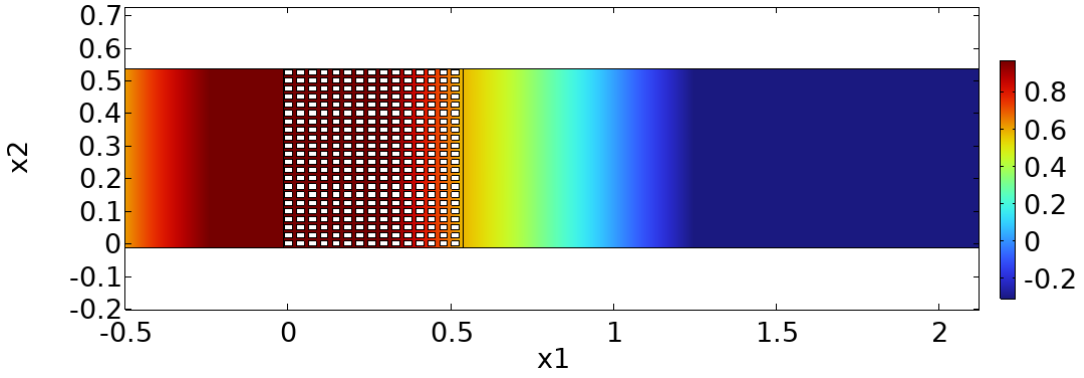

(a) full geometry

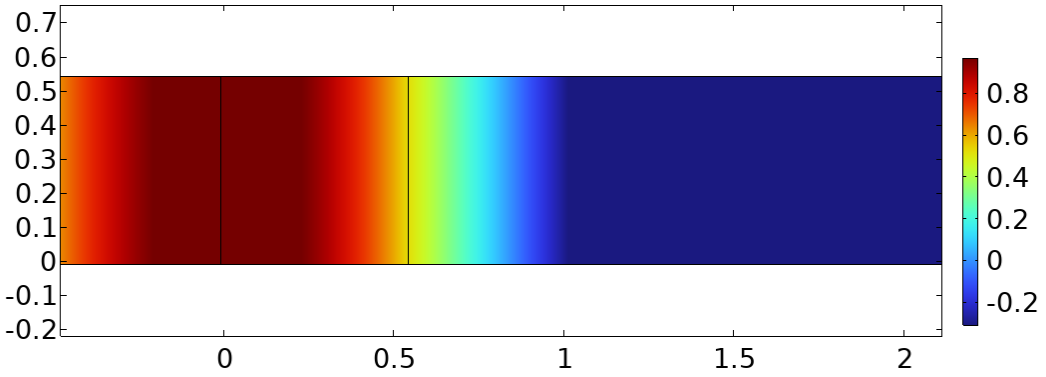

(b) effective medium

Figure 3.16: Matrix of rectangular prisms

The trend just described is present also for 3.16, but the approximation is less effective for the matrix of rectangular prisms (this is evident, for example, comparing where the 0 is for the matrix and for the model in figures 3.15 and 3.16).

-p_i:

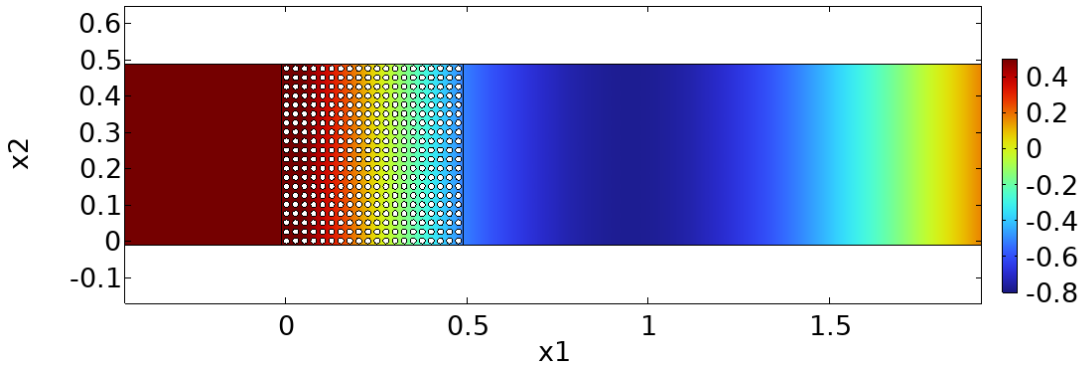

(a) full geometry

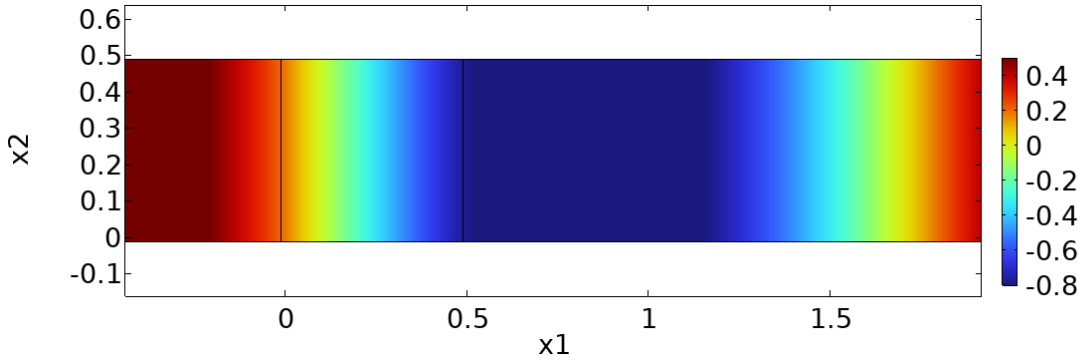

(b) effective medium

Figure 3.17: Matrix of rigid cylinders

The sinusoid for the imaginary part is even more noticeable: p_i grows until the scatterer region, then it decreases, and it increases again before reaching the end of the geometry.

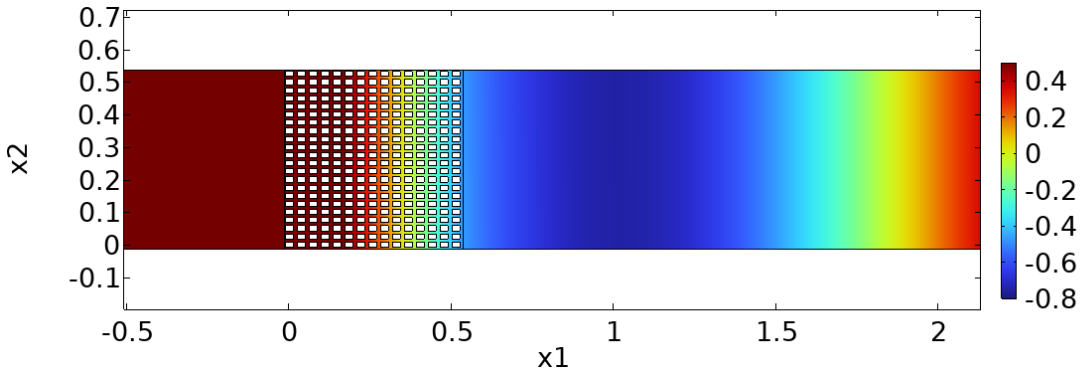

(a) full geometry

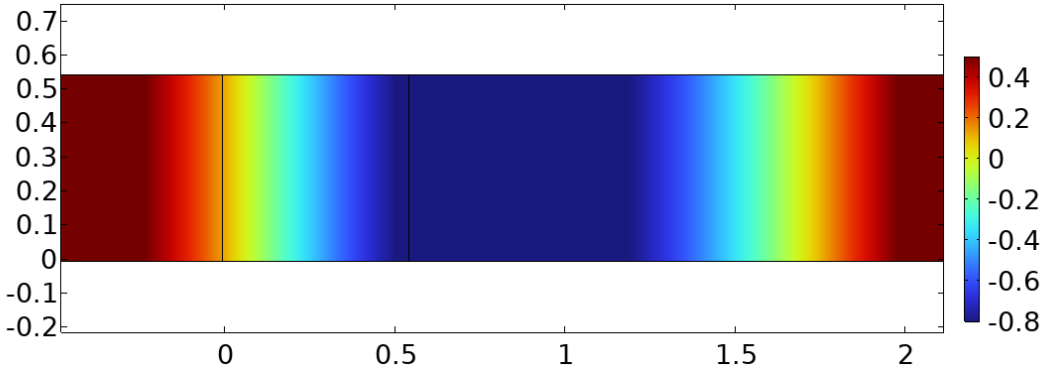

(b) effective medium

Figure 3.18: Matrix of rectangular prisms

Again, the non-isotropic case model does not fit well the real problem, as shown by the higher amplitude of the wave in fig. 3.18(b) rather than in fig. 3.18(a) (the values reached are lower) and by the difference in the phase.

For $f = 200Hz$:

-p_r:

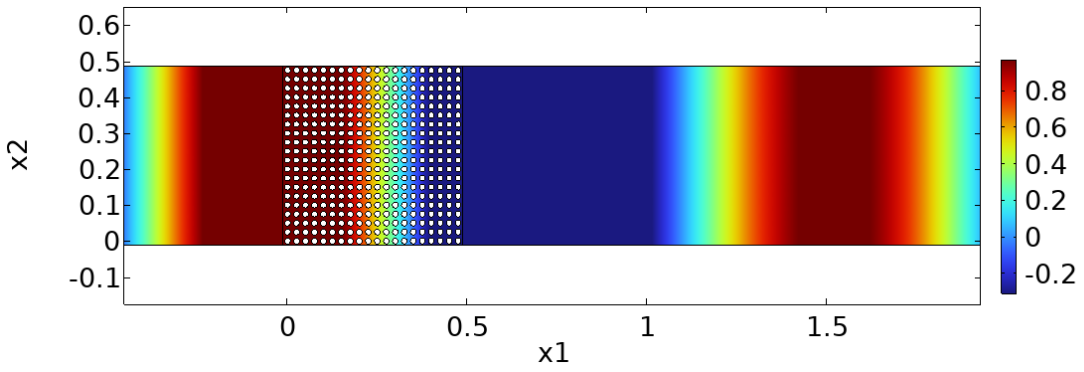

(a) full geometry

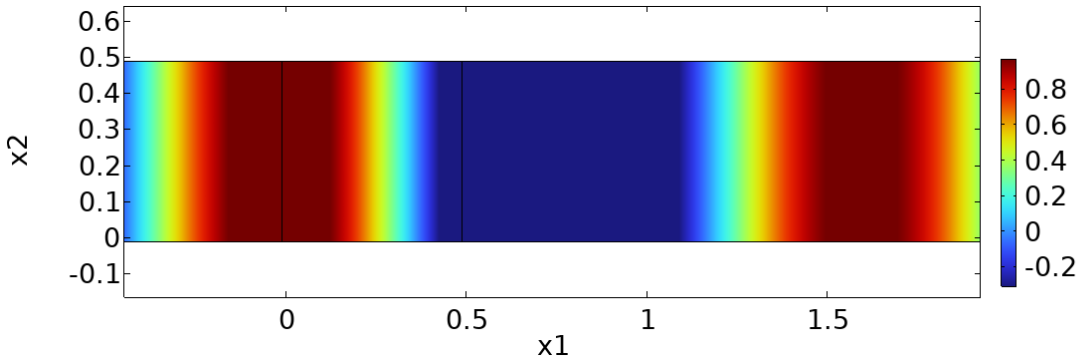

(b) effective medium

Figure 3.19: Matrix of rigid cylinders

For $f = 200Hz$ the sinusoidal behavior of p_r is even more evident: here two peaks of the wave are visible, meaning that a full period period is shown. This is the consequence of a shorter wave length.

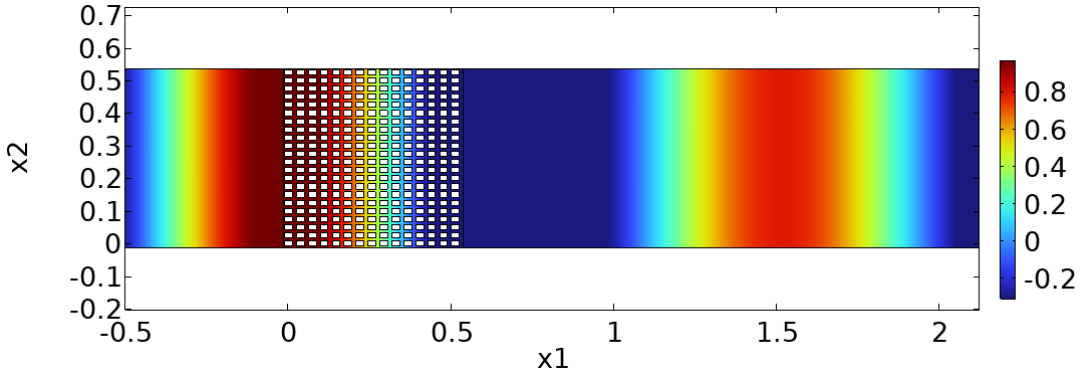

(a) full geometry

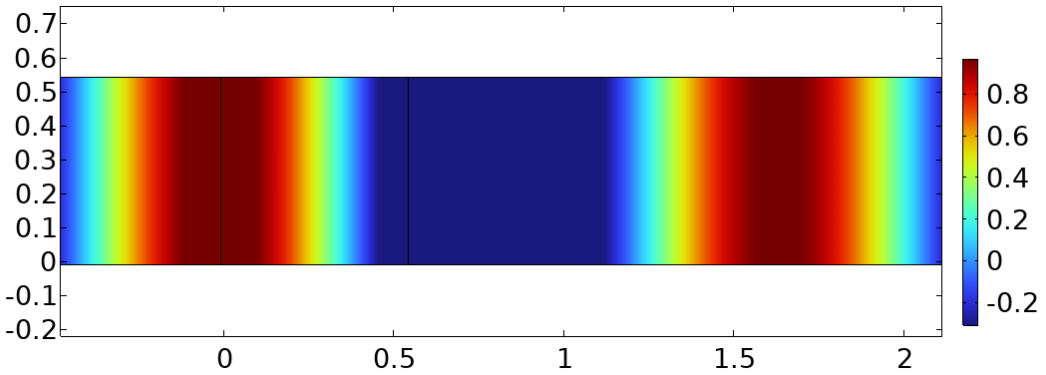

(b) effective medium

Figure 3.20: Matrix of rectangular prisms

In the figure above it is evident the failure of the model: in reality, when the acoustic wave permeates through the matrix, its amplitude decreases drastically as shown in fig. 3.20(a), where the colors suggest that the value of the second peak is lower than the first one.
This phenomenon is not reflected in fig. 3.20(b), where the two peaks have almost the same value.

-p_i:

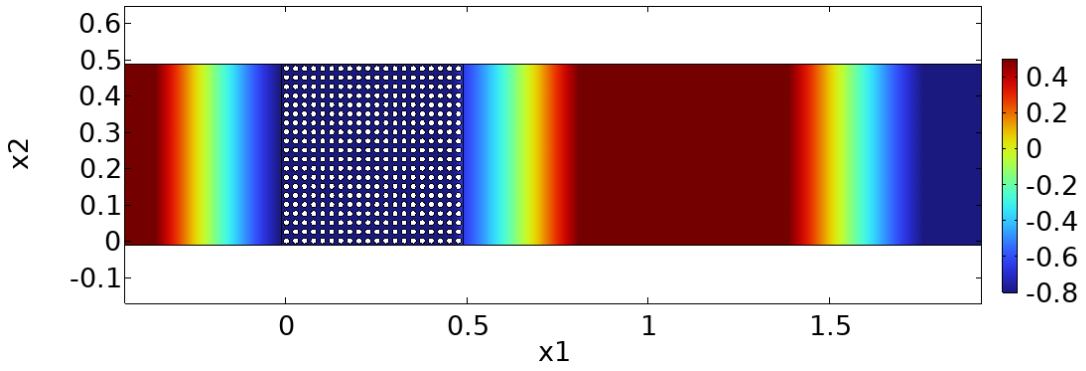

(a) full geometry

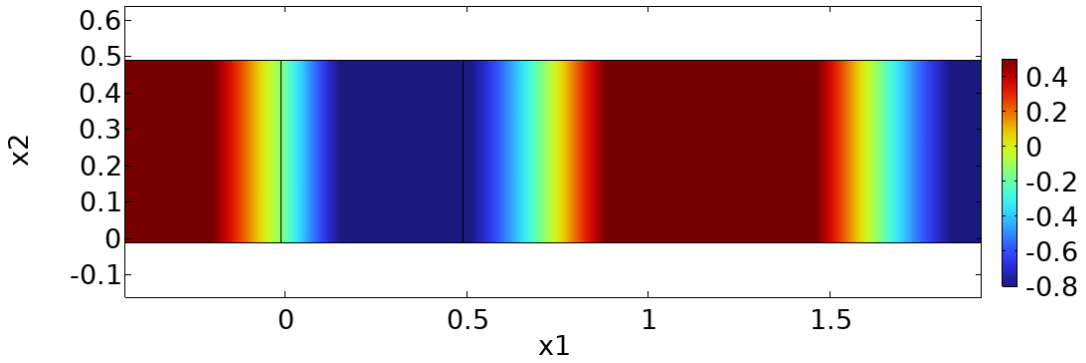

(b) effective medium

Figure 3.21: Matrix of rigid cylinders

However, as already suggested, the model approximation is better for the imaginary part of $p_0^{*\ -ikx}$. The most evident difference between 3.21(a) and 3.21(b) is the gap between the phases, while the amplitude remains almost the same.

For the non-isotropic problem, again, the figures show a less effective approximation given by the model:

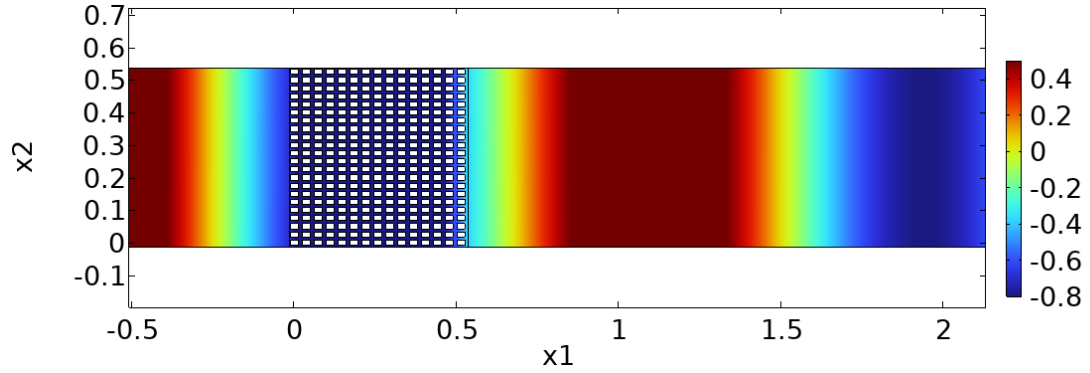

(a) full geometry

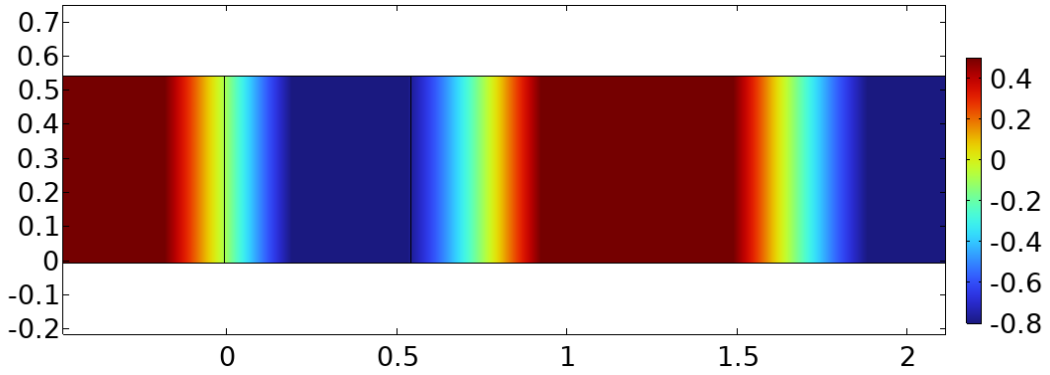

(b) effective medium

Figure 3.22: Matrix of rectangular prisms

The following graphs show the plot of the real part of $p_0^{*\,-ikx}$ for $f = 50Hz$, $f = 100Hz$ and $f = 200Hz$, studied in the previous paragraph, and a comparison with two extreme cases, $f = 20Hz$ and $f = 1000Hz$. The results show how the wave number k, defined as

$$k = \frac{2\pi f}{c_0} \tag{3.2}$$

influences the approximation and, furthermore, whether or not a higher porosity gives a better result. At the beginning, the porosity is the same used in the previous models 3.11 3.12, then, ϕ is increased to a number closer to the unity.

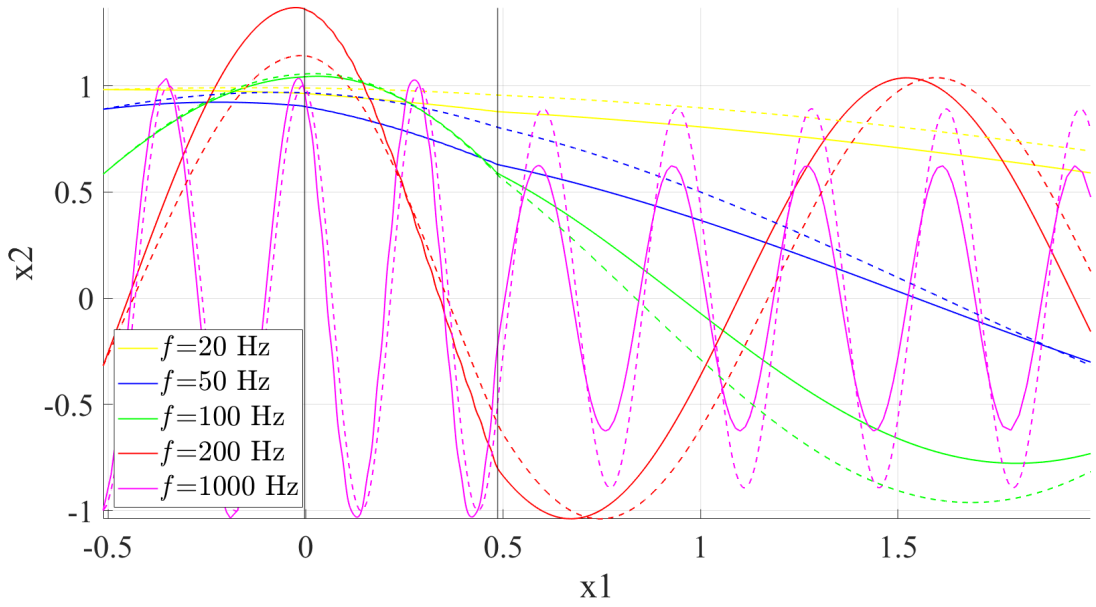

(a) Rigid cylinders, ϕ=0.6783

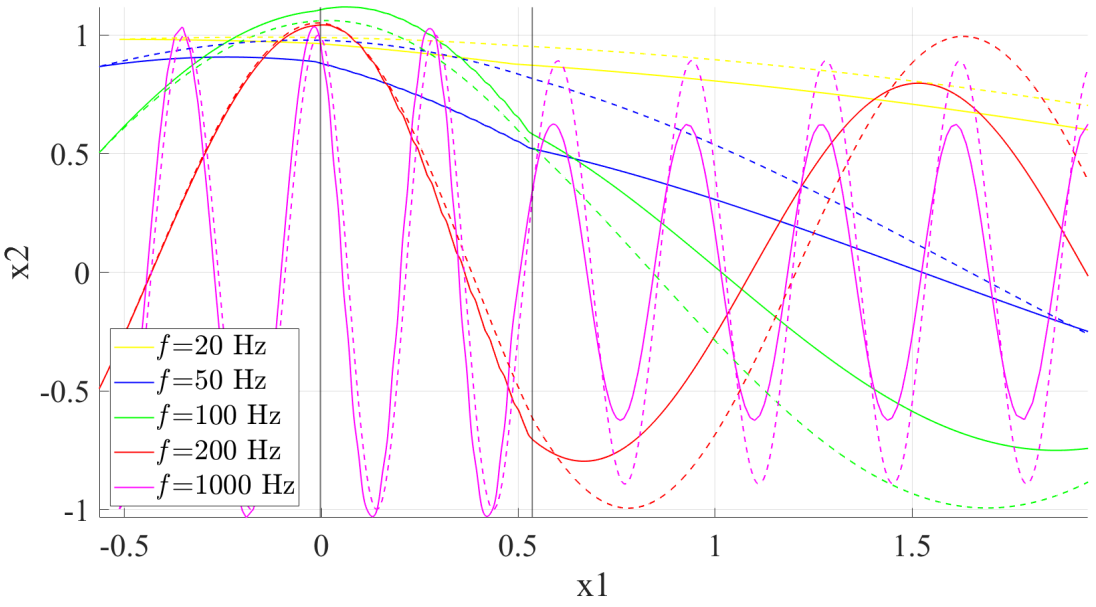

(b) Rectangular prisms, ϕ=0.5811

Figure 3.23: Low porosity. Full lines) real case, dashed lines) model

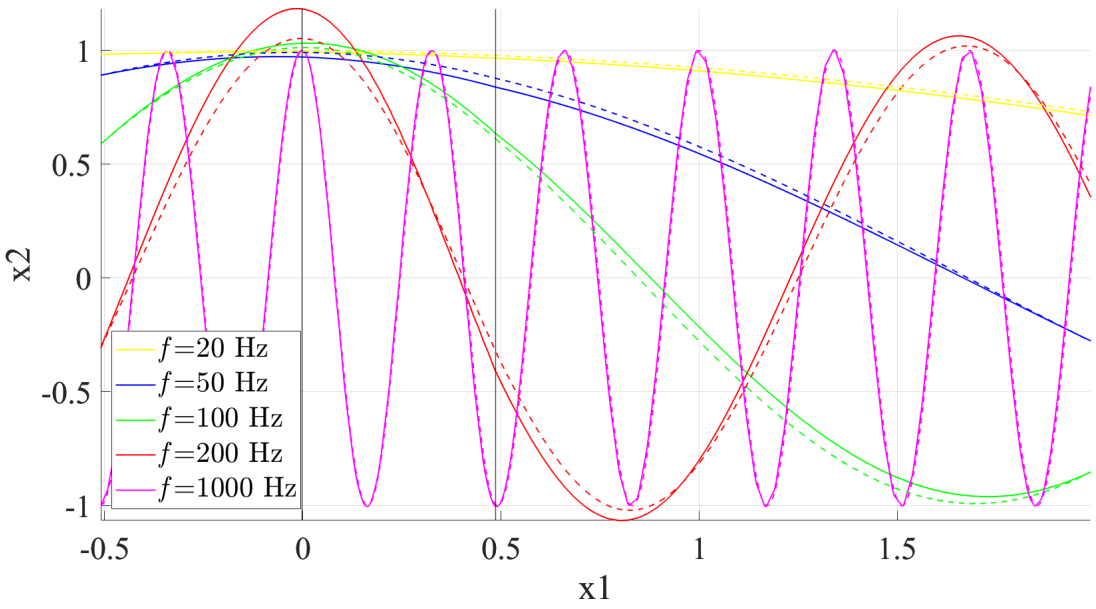

(a) Rigid cylinders, ϕ=0.9196

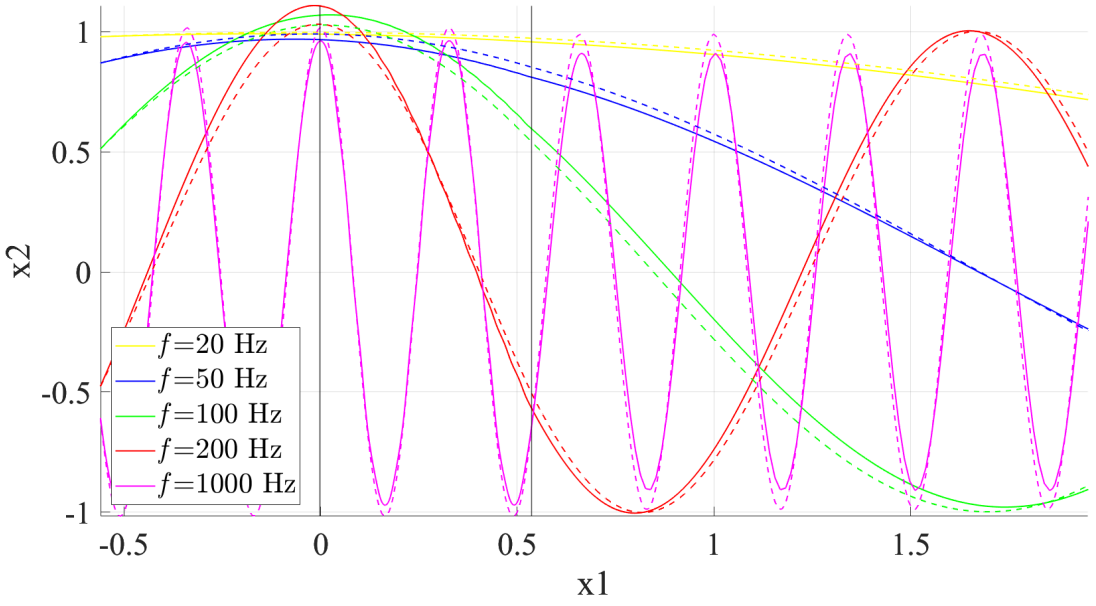

(b) Rectangular prisms, ϕ=0.8953

Figure 3.24: High porosity. Full lines) real case, dashed lines) model

From the observation of the previous graphs, the first thing to notice is that a higher porosity influence positively the effectiveness of the model: the comparison between fig. 3.23 and 3.24 shows an almost perfect match of the functions of the effective medium over the full geometry. This is especially true if the case is isotropic: in fig. 3.24(a) the model is valid for all the frequencies studied.

Later, the focus is on the importance of the wave number: from the analysis of figure 3.23, in particular, it is clear that the approximation fails if the frequency grows, especially after the wave has passed the model block and the matrix (for $f = 1000Hz$, for example, the amplitude of the wave reduces drastically).
Moreover, for both higher and lower porosity, the discrepancy between the effective media and the real cases is even more pronounced when the case is non-isotropic (3.23(b) and 3.24(b)).

We can notice that for the full geometry in figures 3.23, the lines are not exactly straight due to the presence of the cylinders and rectangles. Meanwhile, for figures in 3.24, the behavior of the pressure is more linear. This could be due to the fact that a higher porosity means a smaller solid region, therefore the interference of the array is less pronounced.

Lastly, the difference between the models and the full geometry is also influenced by the lack of the interface condition: for low-frequency cases, the approximation of the model is better so the discrepancy is due to the interface error, for high-frequency cases, the error is due to both lack of interface and failure of the effective medium.

In conclusion, the effectiveness of the model increases when the wave number (or the frequency) decreases and when the porosity grows: however, when the problem is non-isotropic, it is necessary to verify its validity and, if the problem allows it, modify the parameters just mentioned.

Conclusions

The importance of porous materials lies in their wide range of applications, from the natural world to man-made devices. One of the most important applications is acoustic absorption. This thesis aimed to investigate a prototypical two-dimensional acoustic liner material with periodic microstructure: arrays of acoustic-rigid cylinders. We have developed a mathematical model with the homogenization method to describe the global behavior and macroscopic phenomena when acoustic waves are transmitted through the micro-cylinders.

The frequency-domain acoustic wave equation has been derived from the mass, momentum, and energy conservation equations. Zero external mass and forces were added to the system, and the viscous effect was neglected. Then, the governing equation was normalized with chosen dimensionless groups, and the upscaling technique - the homogenization method, was applied. By introducing the parameter $\epsilon = l/L \ll 1$, we separated the length scales and obtained governing equations in different orders of scales. The averaging theorem was applied to the microscale problem and the closure variables were solved in a unit cell. In the end, we obtained a macroscopic model with a second-order tensor parameter, β_{ij}, calculated for isotropic (circular cylinders) and non-isotropic (rectangular cylinders) scatterer shapes at different porosity. For the isotropic case, $\beta_{ij} = \beta\delta_{ij}$. Therefore, only scalar β is needed to be calculated. For the non-isotropic case, the two diagonal components have different values. β_{ij} are also calculated for different aspect ratios. It revealed that maintaining the same porosity, there was no direct correlation between β_{ij} and the aspect ratio.

In the end, the model is validated by finite-element simulations of a case when an incident plane wave is transmitted through the sample material located in the middle of a duct. The numerical simulations were conducted with commercial software COMSOL Multiphysics®. We compared the acoustic pressure field of a fully resolved simulation and a case when the sample was replaced by effective media where the acoustic waves are governed by the developed macroscopic model. The simulations are conducted for different porosity and various frequencies ($f =$ 20 Hz $\sim$ 1000 Hz) of the incident waves. It has been shown that good agreement between the model and full-geometry simulation appears for low-frequency waves. The small discrepancies are due to a lack of treatment at the interface between the free field and the scatterer region. For high-frequency incident waves ($f =$

1000 Hz), the large discrepancy of the pressure fields shown in comparison was mainly due to the failure of the long-wave assumption.

Bibliography

[1] Kuczmarski, M. A. and Johnston, J. C. (2011) Acoustic absorption in porous materials. *NASA/TM,* **216995**.

[2] Bolton, J Stuart, K. Y. J. (1997) Elastic porous materials for sound absorption and transmission control. *SAE transactions,* pp. 2576–2590.

[3] Zvolenskỳ, P., Grenčík, J., Kašiar, L., and Stuchlỳ, V. (2018) Simulation of sound transmission through the porous material, determining the parameters of acoustic absorption and sound reduction. In *MATEC Web of Conferences* EDP Sciences Vol. 157, p. 02058.

[4] Cucharero, J., Hänninen, T., and Lokki, T. (2020) Angle-dependent absorption of sound on porous materials. In *Acoustics* MDPI Vol. 2, pp. 753–765.

[5] Sugimoto, R., Murray, P., and Astley, R. J. (2012) Folded cavity liners for turbofan engine intakes. In *18th AIAA/CEAS Aeroacoustics Conference (33rd AIAA Aeroacoustics Conference)* p. 2291.

[6] Huff, D. L. (2007) Noise reduction technologies for turbofan engines. In *35th International Congress and Exposition on Noise Control Engineering (INTER-NOISE 2006)* Number E-15787.

[7] Liu, X., Zhao, D., Guan, D., Becker, S., Sun, D., and Sun, X. (2022) Development and progress in aeroacoustic noise reduction on turbofan aeroengines. *Progress in Aerospace Sciences,* **130**, 100796.

[8] Ligurskỳ, T. and Michalec, Z. Modelling HM Processes in Porous Media PhD thesis The Czech Academy of Sciences, Institute of Geonics (2020).

[9] Nakayama, A., Ando, K., Yang, C., Sano, Y., Kuwahara, F., and Liu, J. (2009) A study on interstitial heat transfer in consolidated and unconsolidated porous media. *Heat and Mass Transfer,* **45**, 1365–1372.

[10] Dullien, F. A. (2012) Porous media: fluid transport and pore structure, Academic press, .

[11] Mei, C. C. and Vernescu, B. (2010) Homogenization methods for multiscale mechanics, World scientific, .

[12] Touboul, M. Acoustic and elastic wave propagation in microstructured media with interfaces: homogenization, simulation and optimization PhD thesis Aix-Marseille Université (2021).

[13] Nguyen, V. P., Stroeven, M., and Sluys, L. J. (2011) Multiscale continuous and discontinuous modeling of heterogeneous materials: a review on recent developments. *Journal of Multiscale Modelling,* **3**(04), 229–270.

[14] Bottaro, A. (2019) Flow over natural or engineered surfaces: an adjoint homogenization perspective. *Journal of Fluid Mechanics,* **877**, P1.

[15] Rienstra, S. W. and Hirschberg, A. (2004) An introduction to acoustics. *Eindhoven University of Technology,* **18**, 19.